Supporting Information

Edge Activation of Inert Polymeric Carbon Nitride Matrix with Boosted Absorption Kinetic and Near-infrared Response for Efficient Photocatalytic CO_2 Reduction

Qiong Liu[a,b]*, Zhongxin Chen[b], Weijian Tao[c], Haiming Zhu[c], Linxin Zhong[a], Fuxian Wang[d], Ren Zou[a], Yongqian Lei[d], Cuibo Liu[b], Xinwen Peng[a]*

[a]State Key Laboratory of Pulp and Paper Engineering, South China University of Technology, Guangzhou 510641, China

[b]Department of Chemistry and Centre for Advanced 2D Materials (CA2DM) National University of Singapore, 3 Science Drive 3, Singapore 117543, Singapore

[c]Centre for Chemistry of High-Performance & Novel Materials, Department of Chemistry, Zhejiang University

[d]Guangdong Provincial Key Laboratory of Emergency Test for Dangerous Chemicals, Guangdong Institute of Analysis, Guangzhou 510070, China

Corresponding Author

*E-mail: chmv231@nus.edu.sg (Q. Liu); fexwpeng@scut.edu.cn (X. Peng).

Table of contents

1. Scheme of the preparation process for modified PCN samples

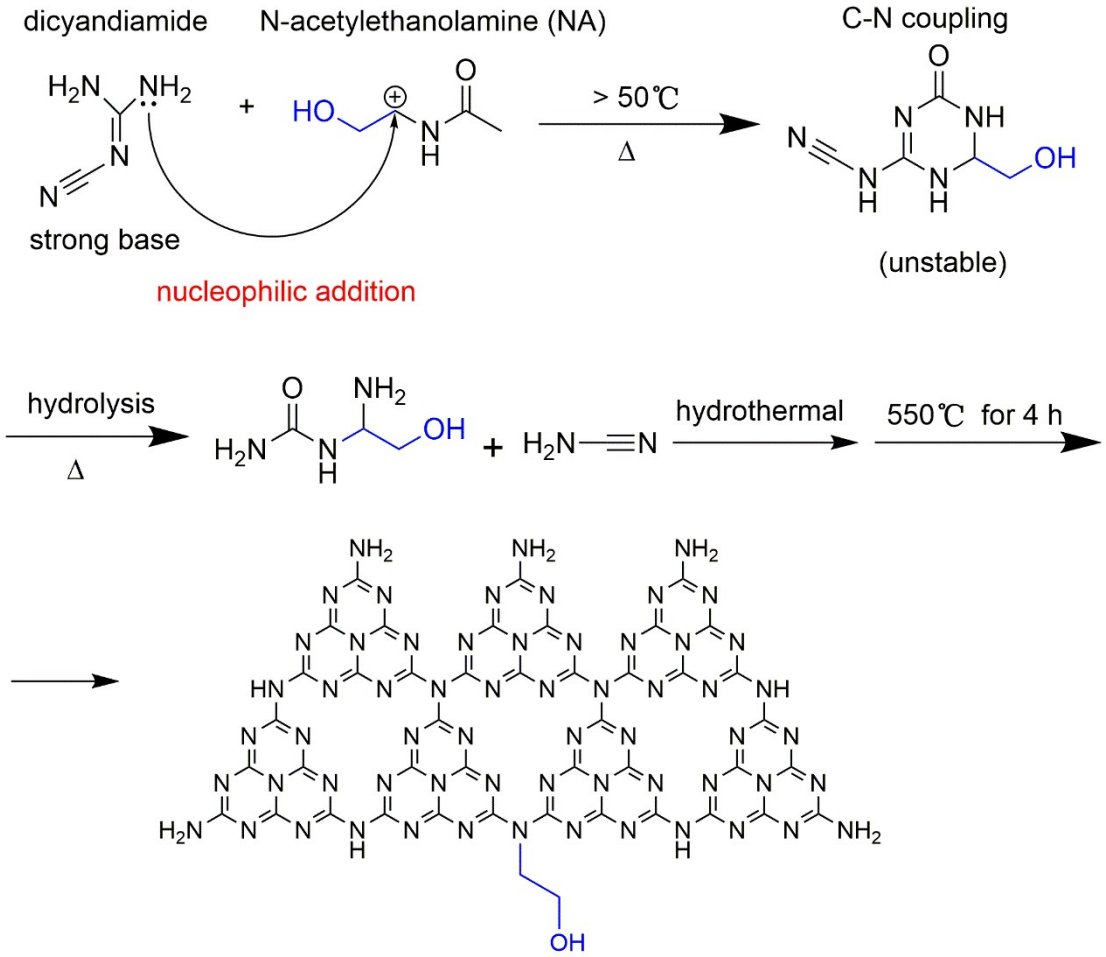

Scheme S1. Tentative reaction mechanism between dicyandiamide and N-acetylethanolamine (NA) via the nucleophilic addition reaction.

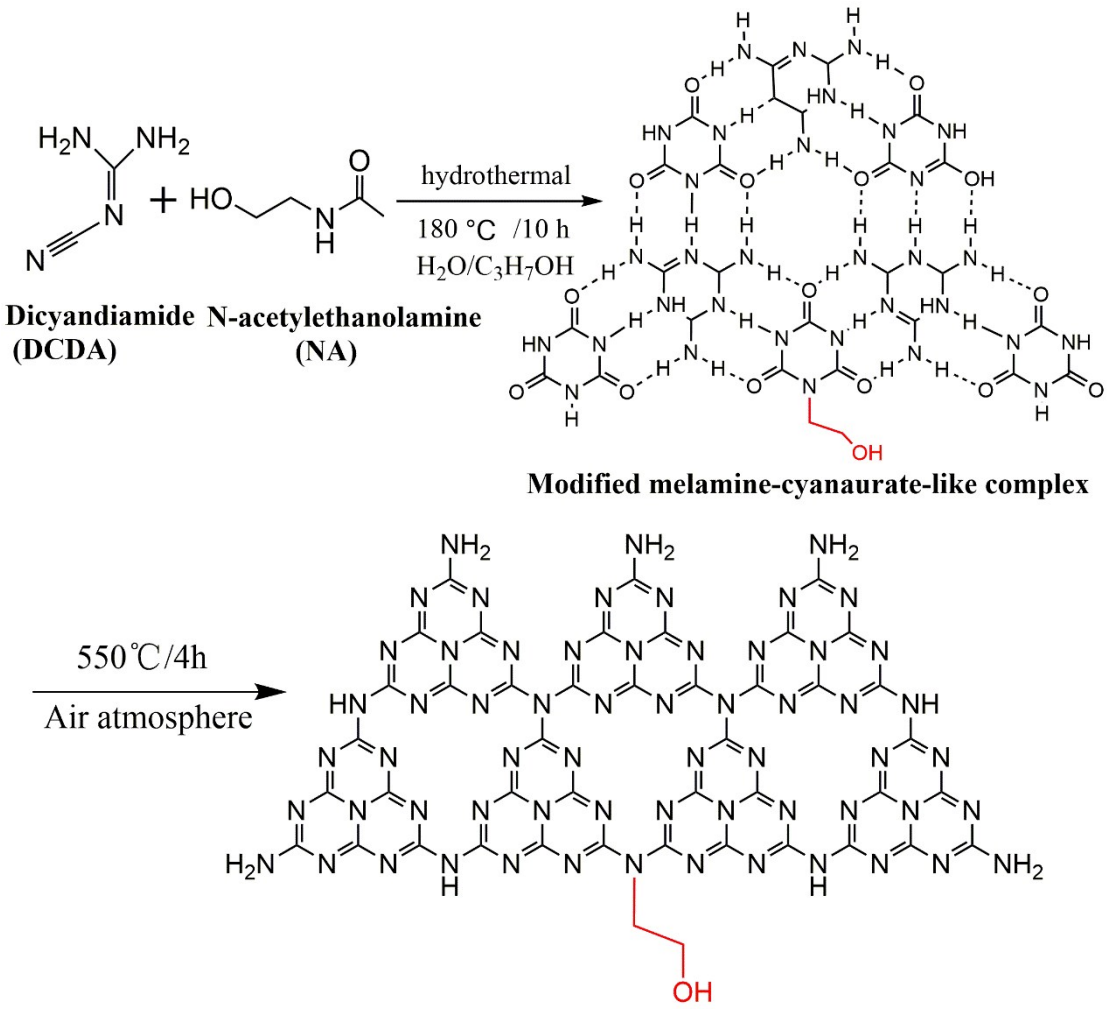

Scheme S2. The synthesized process of CN microtube with hydroxyethyl groups (HCNT-NA), first endured the hydrothermal pretreatment to form into the melamine-cyanurate like complex, then proceeding with high-temperature calcined process to obtain the HCNT-NA. HCN-NA or HCNT was prepared without added propanol or NA under the above same conditions, respectively.

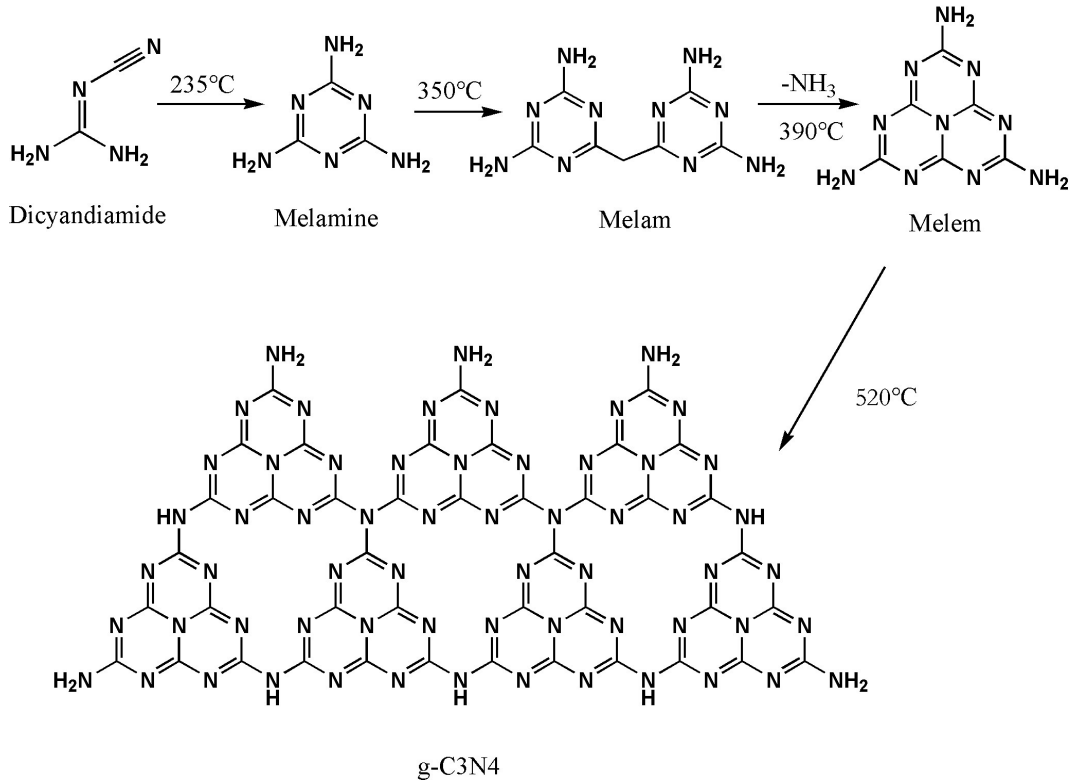

Scheme S3. The typical routes to obtained the bulked g-C_3N_4.

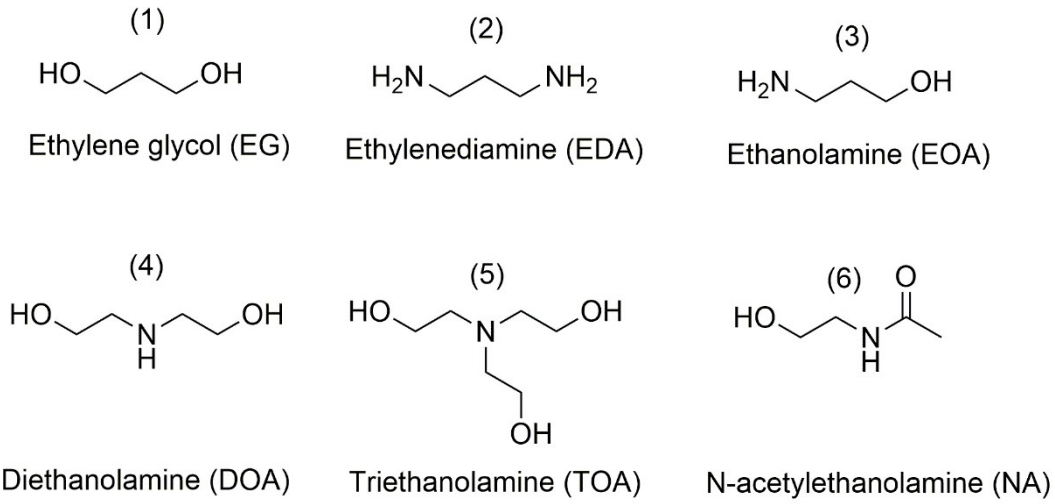

Scheme S4. Selected additive molecule and abbreviated form.

2. Supplementary for chemical structure and morphology (Fig. S1-S10)

Table S1. Physicochemical properties and photocatalytic activities of BCN, HCNT, HCN-NA, and HCNT-NA.

Samples	C/N molar Ratio[a]	S_{BET} (m^2g^{-1})	PV^b (cm^3g^{-1})	Band gap (eV)	O from EA (%)
BCN	0.672	9.5	0.017	2.84	1.563
HCNT	0.661	76.1	0.284	2.90	3.616
HCN-NA	0.709	72.8	0.225	2.81	4.112
HCNT-NA	0.691	73.3	0.258	2.81	4.437

a: data from element analysis (EA); PV^b: Pore Volume.

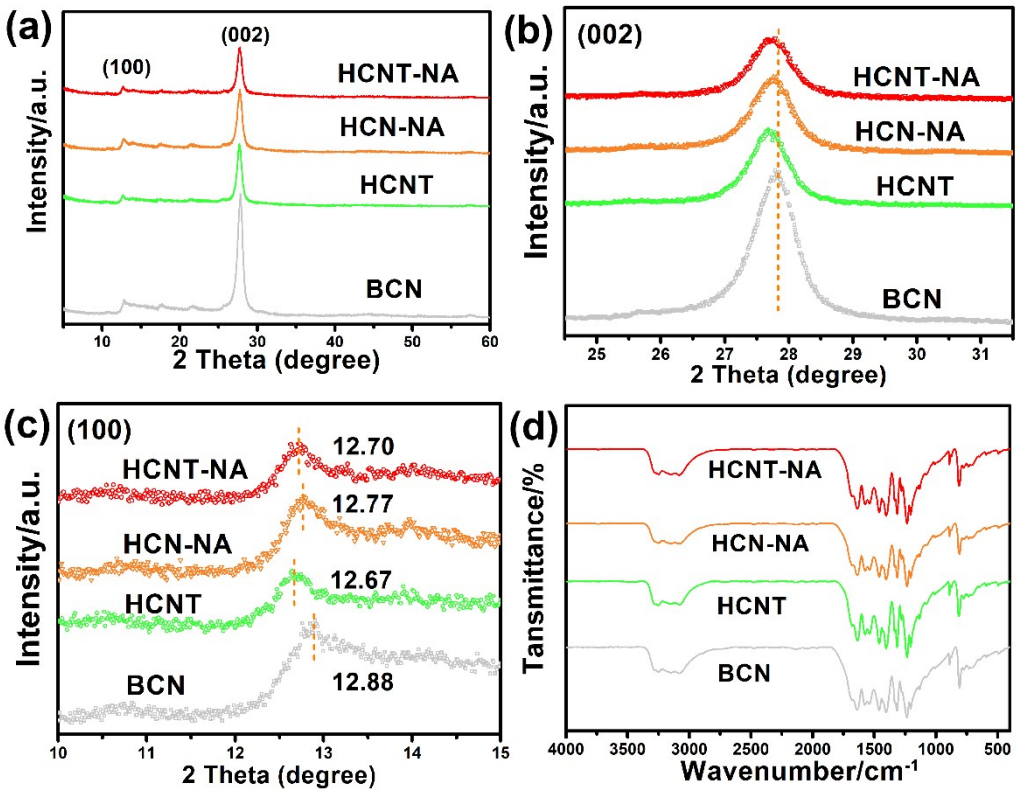

Fig. S1. (a) XRD. (b) Enlarged (002) plane. (c) Enlarged (100) plane and FTIR spectrums of BCN, HCNT, HCN-NA and HCNT-NA. BCN is named from the bulked

(pristine) carbon nitride, HCNT, HCN-NA and HCNT-NA were synthesized from the dicyandiamide (DCDA) endured the mixture: in water/propanol, water/NA, water/propanol and NA, respectively.

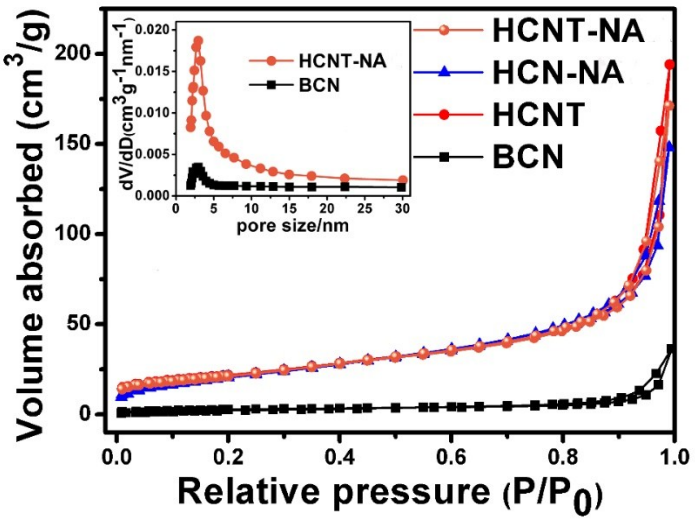

Fig. S2. N_2 adsorption-desorption isotherms of BCN, HCNT, HCN-NA, and HCNT-NA (the inset is their pore size distribution curves of BCN and HCNT-NA).

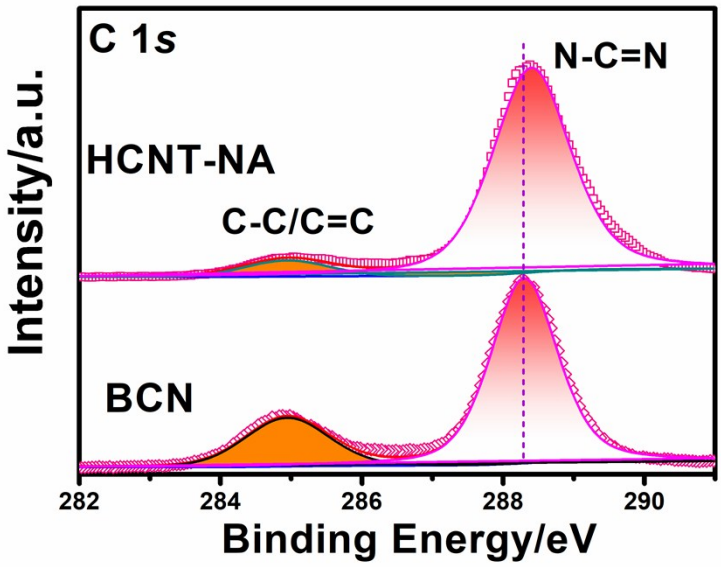

Fig. S3. High-resolution XPS C 1*s* of BCN and HCNT-NA.

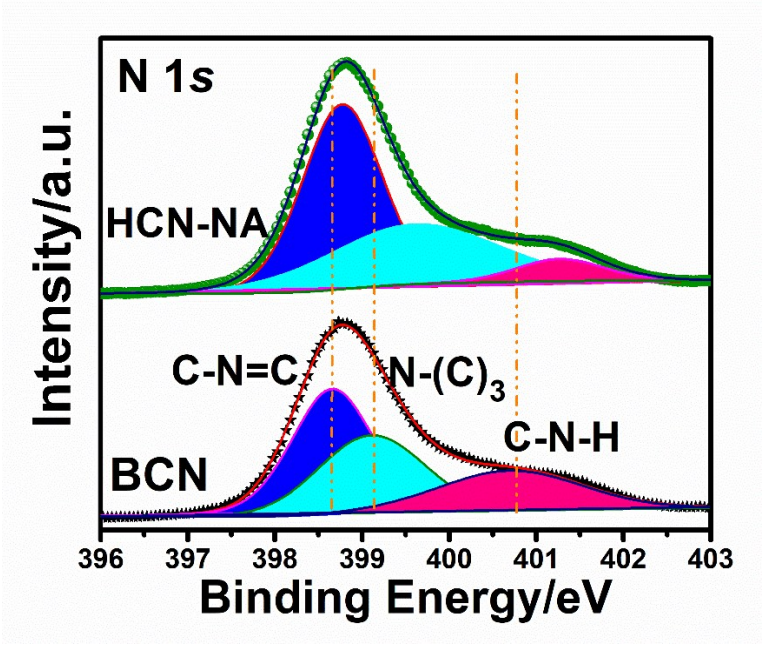

Fig. S4. High-resolution XPS N 1*s* of BCN and HCN-NA. Three different components corresponding to C-N=C, N-$(C)_3$ and C-N-H[3] show the right shift compared to BCN. This shift tendency in HCN-NA is similar to HCNT-NA.

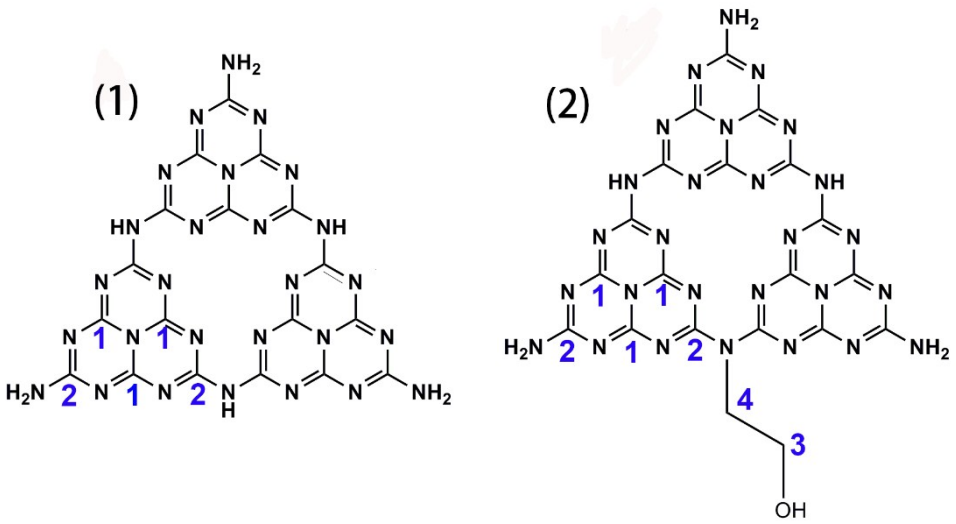

Fig. S5. The corresponding chemical structure related to the solid NMR ^{13}C spectrums.

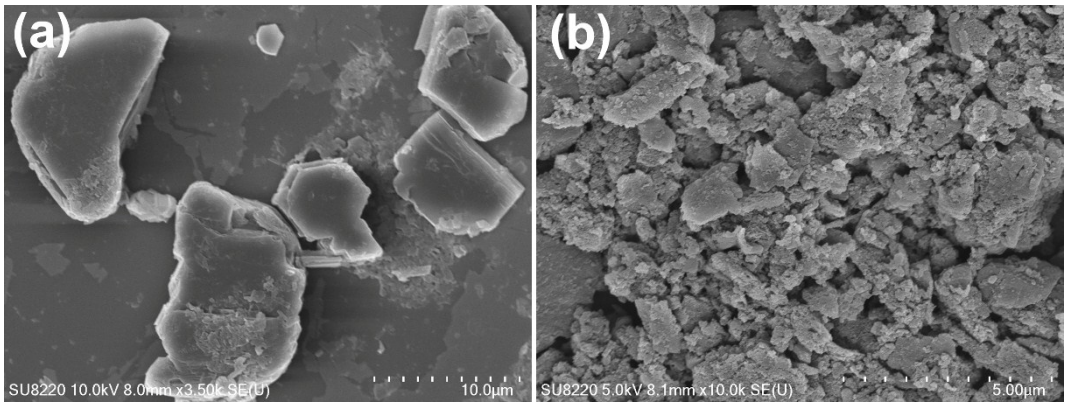

Fig. S6. SEM images of the (a) precursor dicyandiamide (DCDA) and (b) the corresponding bulked Carbon Nitride (BCN). The precursor DCDA just presents the irregular and large particles, after endured the polymerization process, the obtained BCN still retains the irregular bulked morphology.

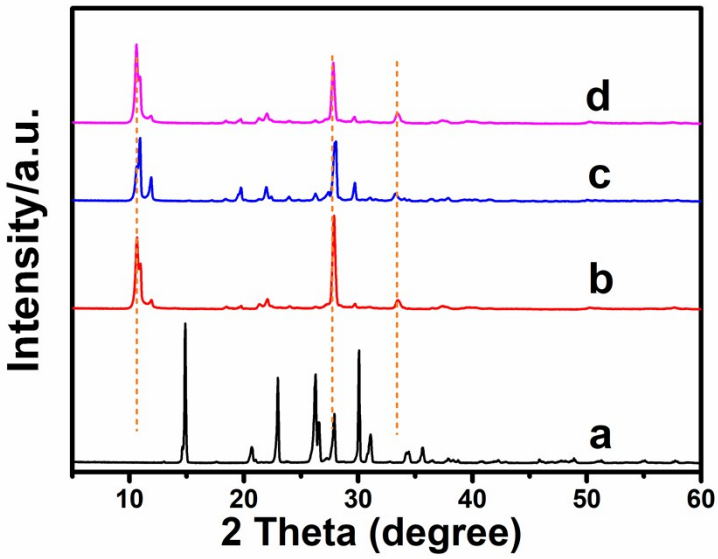

Fig. S7. XRD spectrums of the intermediate of (a) BCN (just the precursor DCDA without any other treatment), (b) HCNT, (c) HCN-NA and (d) HCNT-NA, which the intermediate solids are prepared by hydrothermal treatment with the DCDA in water/propanol, water/NA, water/propanol and NA, respectively.

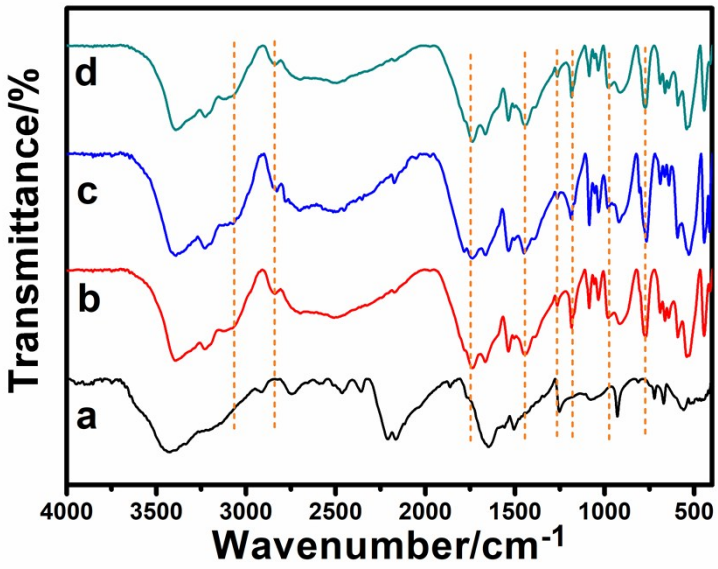

Fig. S8. FTIR spectra of the intermediate of (a) BCN, (b) HCNT, (c) HCN-NA and (d) HCNT-NA.

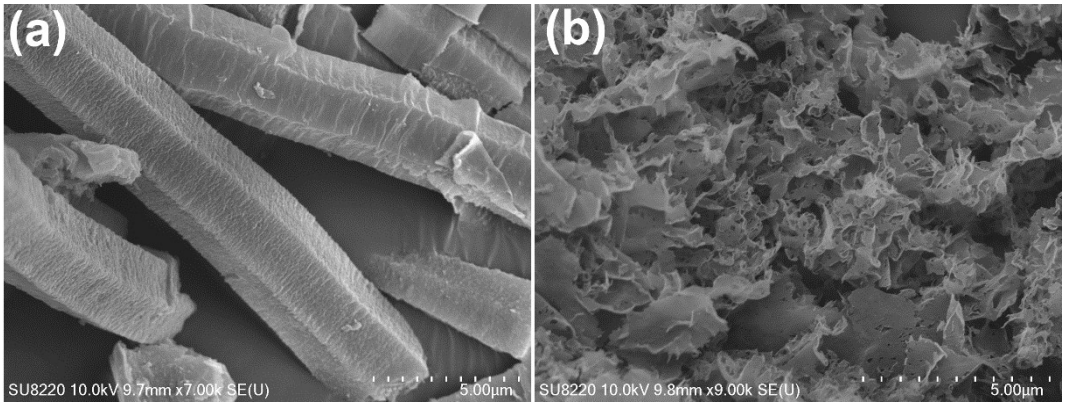

Fig. S9. SEM images of (a) HCNT and (b) HCN-NA.

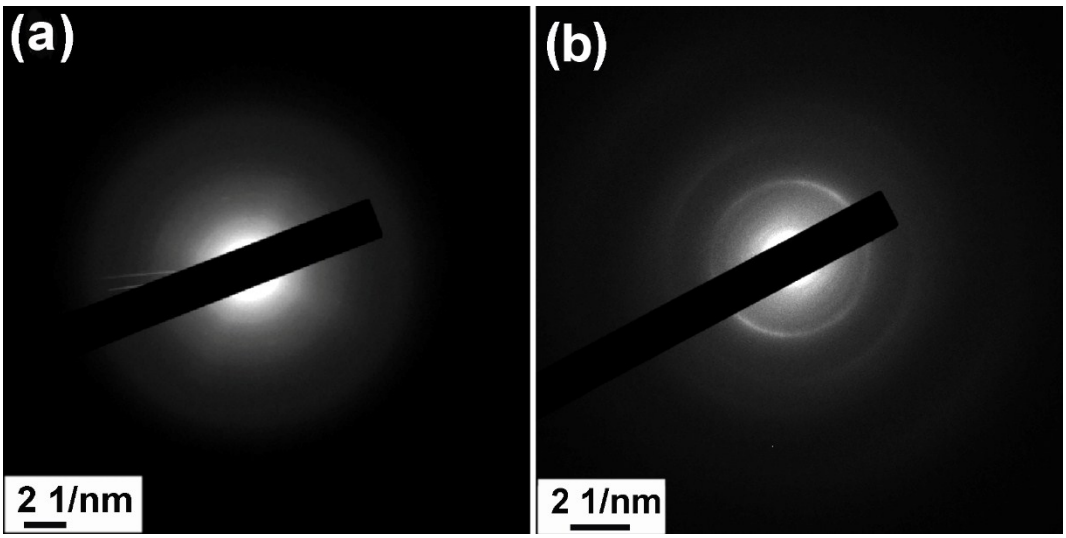

Fig. S10. Selected area electron diffraction (SAED) patterns of (a) HCNT and (b) HCN-NA.

3. Supplementary for electronic structure and charge separation (Fig. S11-S17)

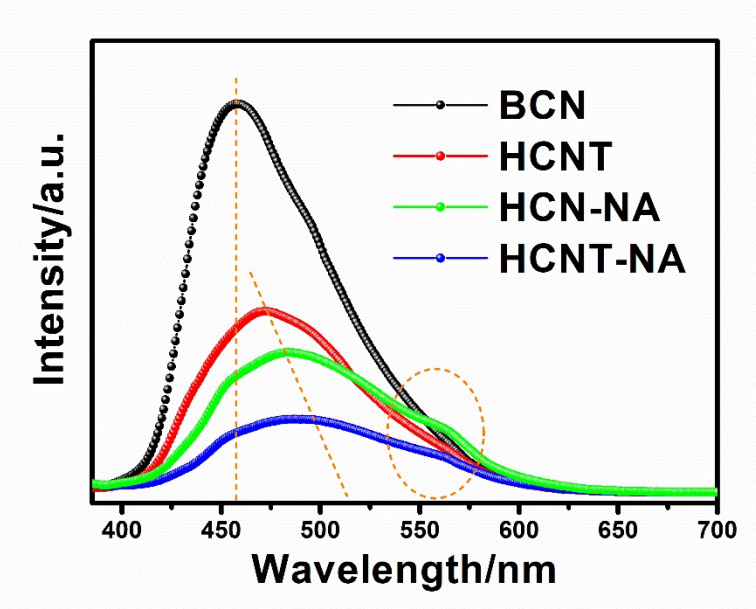

Fig. S11. Photoluminescence (PL) spectrum of BCN, HCNT, HCN-NA, and HCN-NA. Both HCNT, HCN-NA, and HCNT-NA shows the reduced intensity of PL emission peak, also exhibits the red-shift of the peak, the reduced intensity demonstrates the efficiently retarded charge recombination due to the existence of porous structure and the introduction of hydroxyethyl group. And HCN-NA and HCNT-NA further possess the broad shoulder peak among the 550-600 nm, might be originated from the existence of intermediate band in the energy gap and the redistributed localized states, in accord with the DRS results, demonstrating the introduction of hydroxyethyl group could exert a prominent role in tuning the electronic structure and extending the optical absorption region.

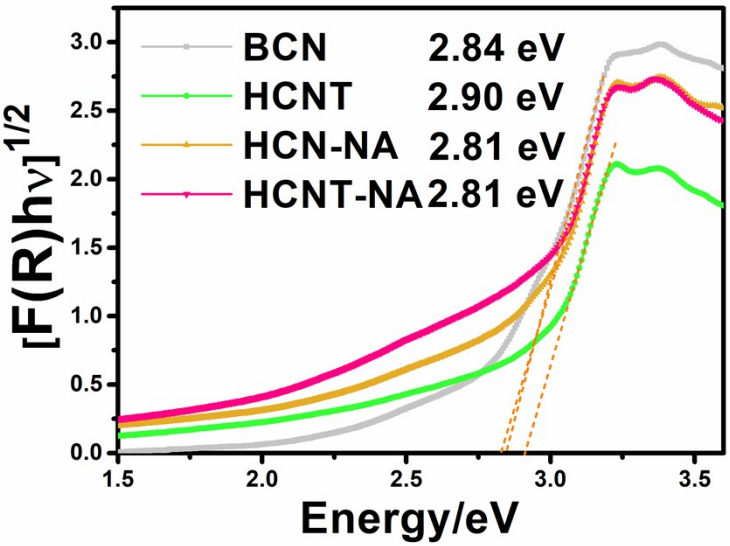

Fig. S12. The calculated band gap of BCN, HCNT, HCN-NA, and HCNT-NA converted using the Kubelk Munk function from Diffuse reflectance UV-Vis spectra.

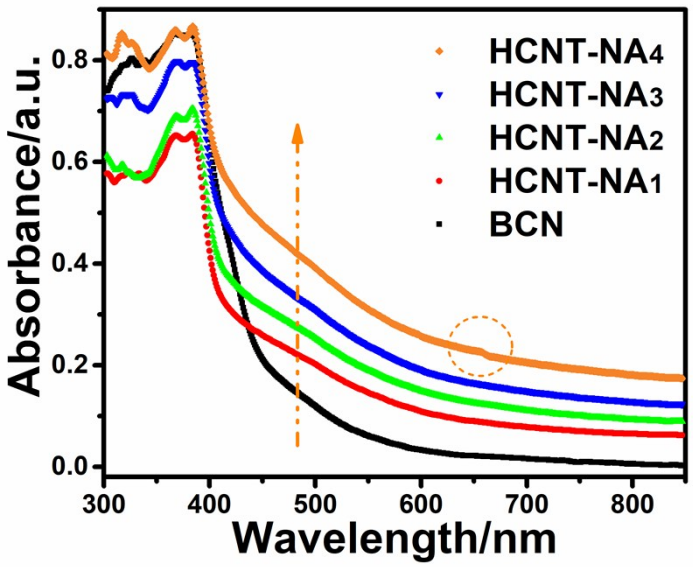

Fig. S13. (a) Diffuse reflectance UV-Vis spectra of a serial of HCNT-NA samples as the different addition content of NA and (b) enlarge DRS spectra from 620-680 nm (note: HCNT-NA_1, HCNT-NA_2, HCNT-NA_3 and HCNT-NA_4 means the addition of NA is 0.05, 0.10, 0.15 and 0.20 mL, if not specified, we use HCNT-NA to signify HCNT-NA_3). As with the addition of NA motif, firstly, the extended optical absorption

region in the resulted samples from 450-780 nm of the visible light region and 780-850 nm of parts of the near-infrared region can be observed, indicating a new discrete energy level with an intermediate photoexcitation state, due to the grafting of hydroxyethyl group. Then, with the progressively increasing the NA content, the apparently enhanced absorption capacity is presented, signifying the existence of the hydroxyethyl group is able to rational modulate the optical absorption region and the electronic structure. A small shower peak at 655 nm is presented in HCNT-NA_4 verifying the formation of the intermediate band, while HCNT-NA using a lower concentration of NA addition was not observed, demonstrating the formation of the intermediate band contributes towards the presence of hydroxyethyl groups.

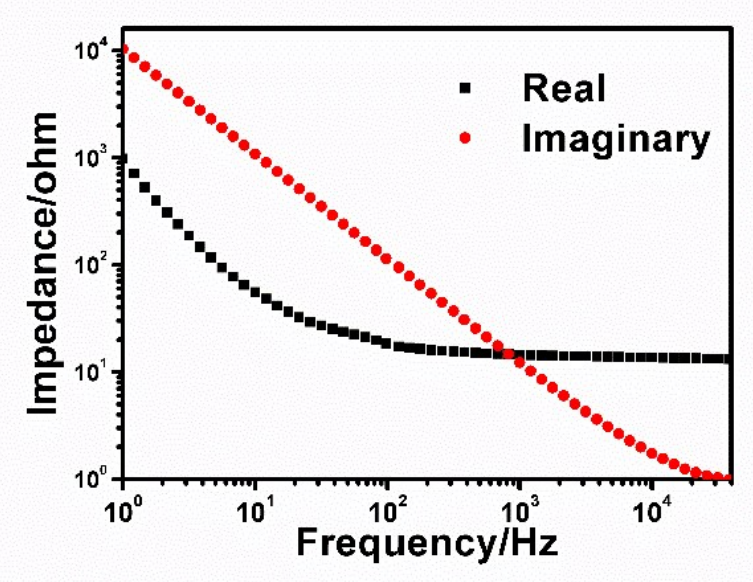

Fig. S14. EIS plots of HCNT-NA in the dark. (Note that, when the frequency above 1000 Hz, the real part of the impedance spectrum renders a nearly constant, and the imaginary part presents a slope of -1. This suggests that this system presents as a resistance in series with a pure capacitance, which serves as the prerequisite to Mott-Schottky analysis. Then we select the 3000, 4000 and 5000 Hz as the test frequency.

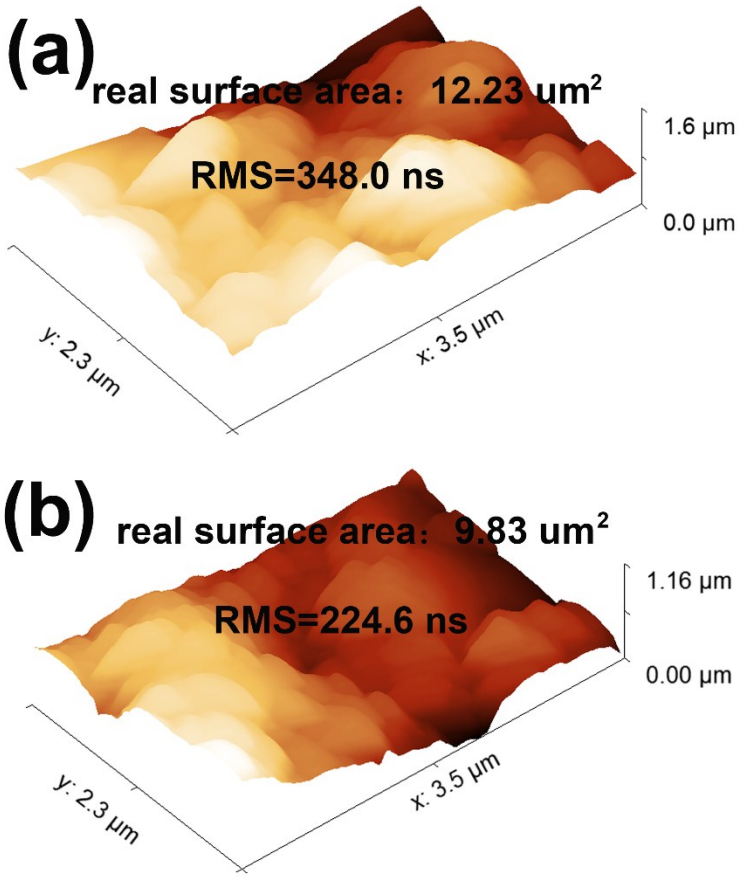

Fig. S15. The surface areas of (a) BCN and (b) HCNT-NA by AFM images for M-S plots. For BCN, the active area is 12.13/ (2.3*3.5) =1.52, and HCNT-NA is 9.83/ (2.3*3.5) =1.22.

The carrier concentration was calculated from the (1)[2]:

$$\frac{1}{C_{SC}^2} = \frac{2}{\varepsilon_0 \varepsilon_r e N_D A^2}\left(\Phi_{SC} - \frac{kT}{e}\right) \quad (1)$$

Where e is the elemental charge: 1.6×10^{-19} C, A is the active area of work electrode, ε_0 is the permittivity of vacuum: 8.85×10^{-14} F/cm, ε is the relative permittivity of the material, the value is 5.5 for C_3N_4. The value of kT/e is too low; it is generally ignored. Hence

$$N_D = \frac{2}{k_1 \times 1.6 \times 10^{-19} \times 8.85 \times 10^{-14} \times 5.5} = k_1^{-1} \times 2.568 \times 10^{31}$$

k_1 is the slope of Mott-Schottky plots, A is the active surface area when we use a 1 cm^2 work electrode. We calculated the slope at the frequency of 4000, for BCN, the slope is $3.4803*10^{10}$; and for HCNT-NA, it has a lower slope of $1.3651*10^{10}$; therefore, we can achieve the carrier donor density that BCN is $7.38 *10^{20}$ cm^{-3} and HCNT-NA is $1.88*10^{21}$ cm^{-3}.

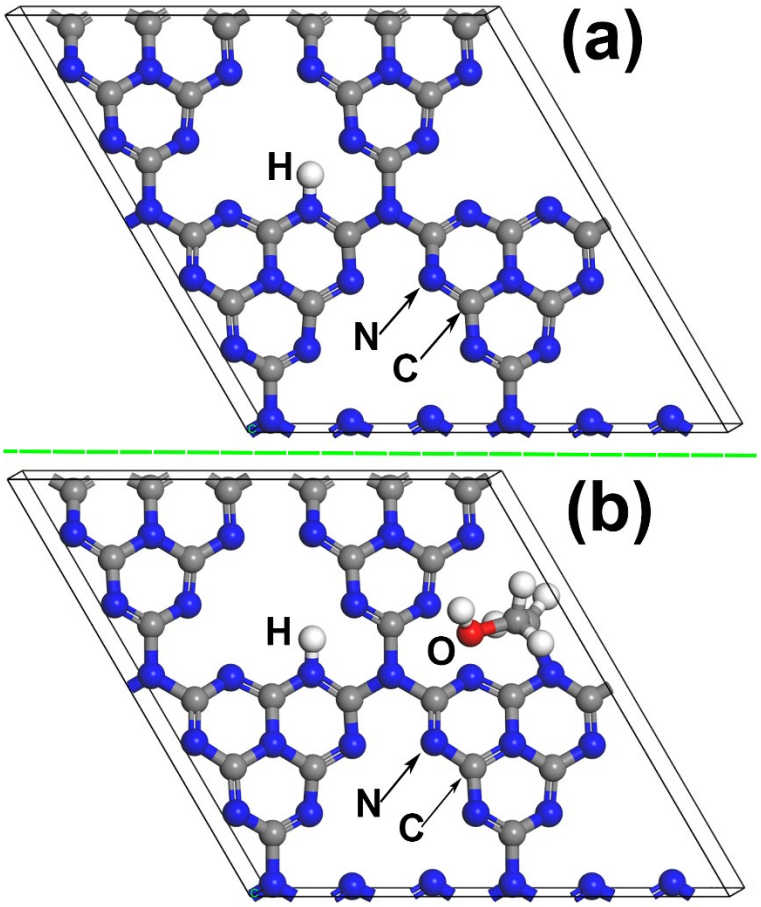

Fig. S16. Structures modes of (a) CN and (b) CN-NA with hydroxyethyl groups.

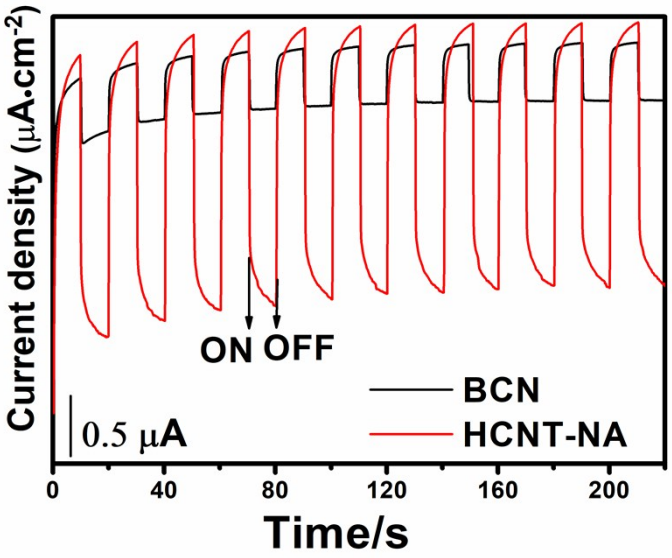

Fig. S17. Periodic ON/OFF photocurrent response in 0.5M Na_2SO_4 electrolyte under visible light irradiation (λ>420 nm) at -0.2 vs. Ag/AgCl electrode, of HCNT-NA and BCN. The transient photocurrents of BCN and HCNT-NA have been measured to investigate the photo-generated charge mobility. As displayed in **Fig. S17**, the obviously enhanced photocurrent value occurs to HCNT-NA and is also reproducible during the several ON/OFF illumination cycles. It means the HCNT-NA possesses the high separation efficiency and the higher concentration of the electron-hole pairs[4].

4. Supplementary for CO2 activity evaluation (Fig. S18-S29)

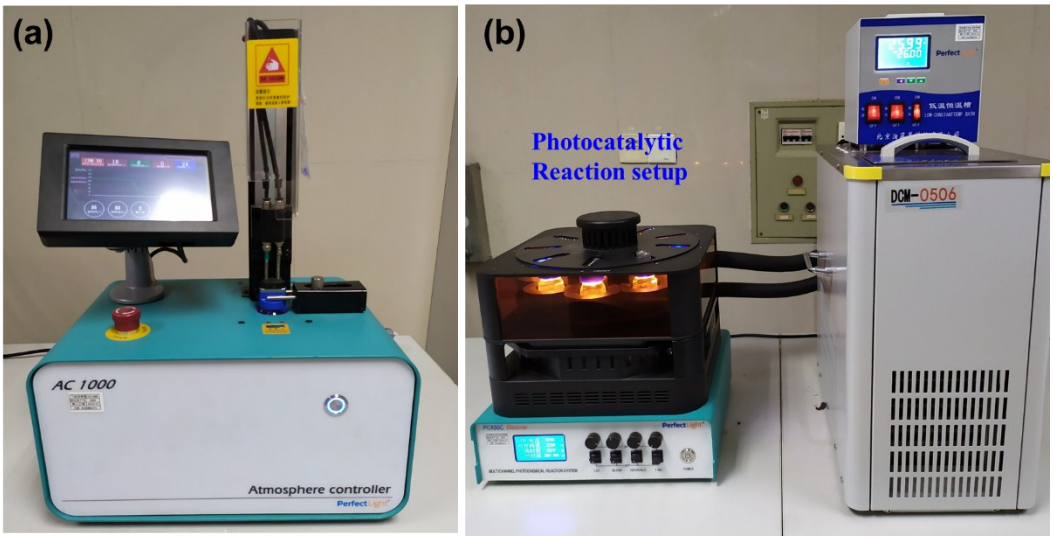

Fig. S18. (a) The atmosphere controller to degas the air and filled into the high pure CO_2 gas into the reactor. (b) The photocatalytic reaction setup.

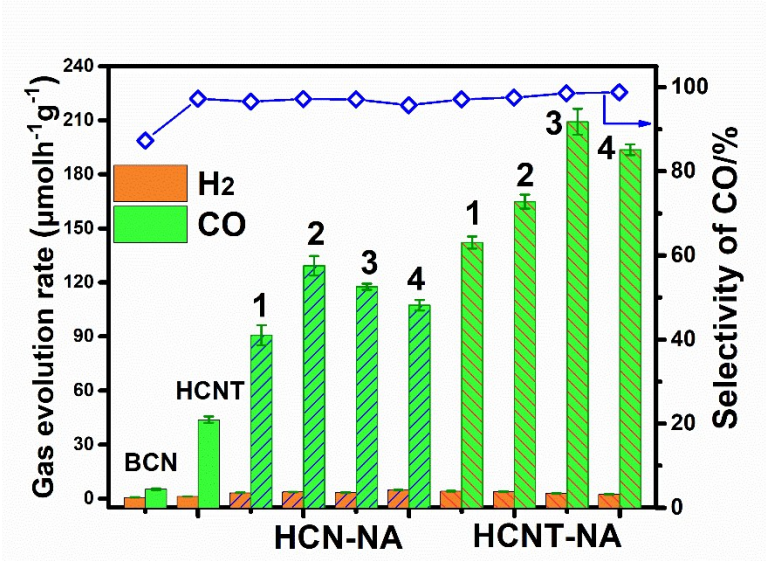

Fig. S19. The average generation rate of CO_2 reduction products using different photocatalyst samples with a corresponding selectivity. (note: HCNT-NA_1, HCNT-NA_2, HCNT-NA_3, and HCNT-NA_4 means the addition of NA is 0.05, 0.10, 0.15 and 0.20 mL, the same as the HCN-NA sample).

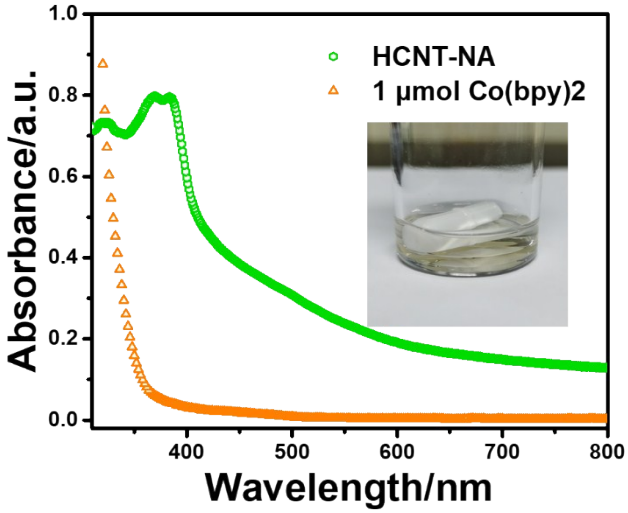

Fig. S20. The UV-Vis absorption spectra of 1 μmol $Co(bpy)_2$ complex (the mixture of $CoCl_2$ and 2, 2-bipyridine, in 2 mL acetonitrile solution) and HCNT-NA. Inset image

is the digital picture of 1 μmol $Co(bpy)_2$ complex in 3.5 ml 10% TOA/acetonitrile/H_2O solution after photocatalytic reaction.

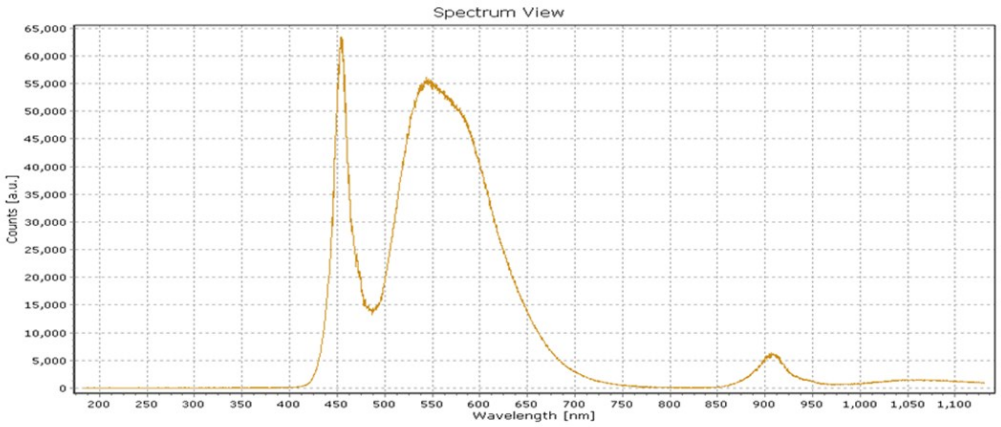

Fig. S21. The optical absorption spectrum of the white LED light source.

The UV-Vis absorption spectra of $Co(bpy)_2$ complex was shown in the Supporting Information **Fig. S20**, together with the HCNT-NA sample. Seen from the **Fig. S20**, the optical absorption spectrum of HCNT-NA almost covers the whole absorption spectrum of $Co(bpy)_2$ complex. 1 μmol $Co(bpy)_2$ complex in the reaction system only could absorb the UV light, while no UV light source is presented in the system, the absorption spectrum of white LED light shown in **Fig. S21**. This result demonstrate the $Co(bpy)_2$ complex is not able to absorb the incident light source and generate the excited carriers to driven the photocatalytic CO_2 reduction reaction. Inset image in **Fig. S20** show $Co(bpy)_2$ complex almost possesses the colorless and transparent status after the photocatalytic reaction.

Control experimental were carried out in **Fig. S22**. Without the addition of Co complex (bipyridine cobalt) in the reaction system, no CO product is generated. While, certain amount of H_2 gas is detected, signifying HCNT-NA serve as the photocatalyst.

The addition of Co complex is necessary for successfully reducing CO_2 to CO. However, if without the addition of photocatalyst of HCNT-NA, the reaction system couldn't generate the CO or H_2 gas, see column 7. Based on these results, We speculate the Co complex in this reaction system serves as the cocatalyst to lower the energy barrier, and the PCN samples serve as the photocatalyst to absorb the white light to generate the excited carriers, then transfer the excited electron to the cocatalyst of Co complex. This is verified by the fluorescence quenching experiments in **Fig. S20**. The addition of Co complex in PCNs dispersion liquid obviously lower the intensity of fluorescence emission peak, suggesting the excited carriers are transferred to complex.

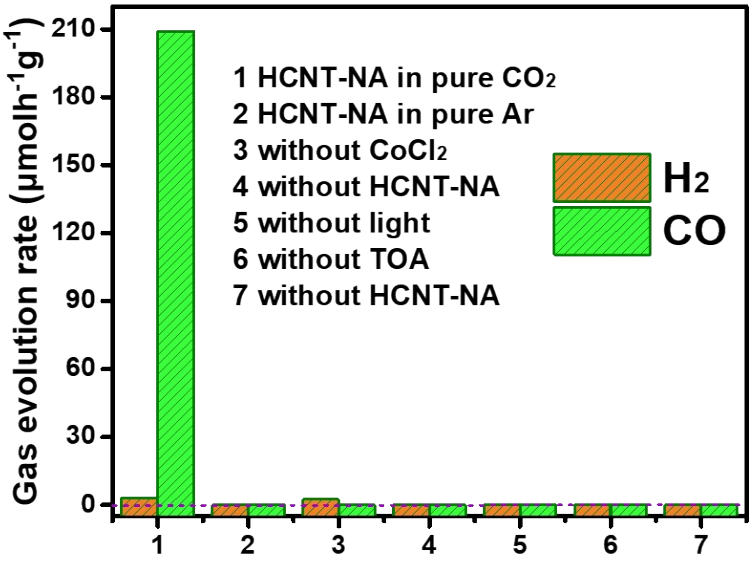

Fig. S22. The average generation rate of CO_2 reduction products under different control conditions. Without the addition of $CoCl_2$, no CO gas is detected, but small amounts of H_2 is observed. Without the addition of HCNT-NA, no product is detected.

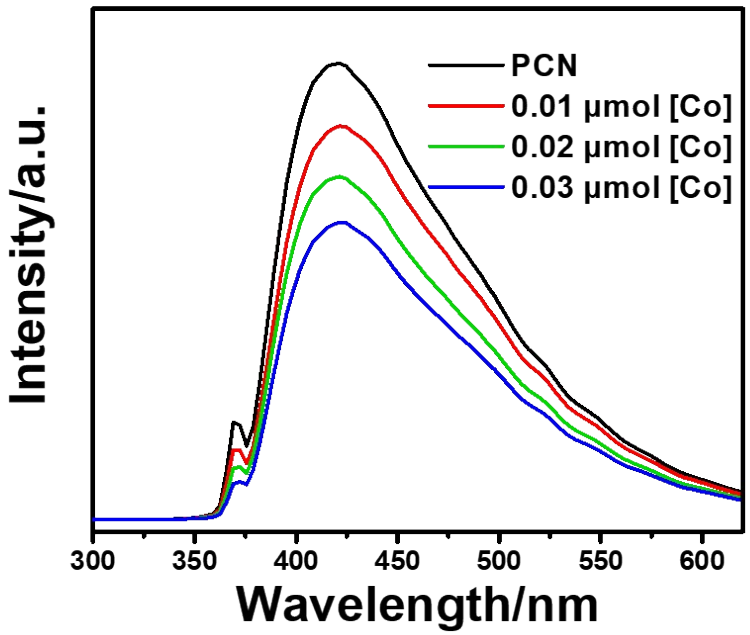

Fig. S23. The Photoluminescence (PL) emission spectra of PCN suspension solution (black line) and PCN with the adding different amounts of Co complex from 0.01 μmol to 0.03 μmol. The PCN (BCN) sample was pretreated by using 2M HCl and stirred at 80 ℃ for 8 h. The excited wavelength is set at 370 nm.

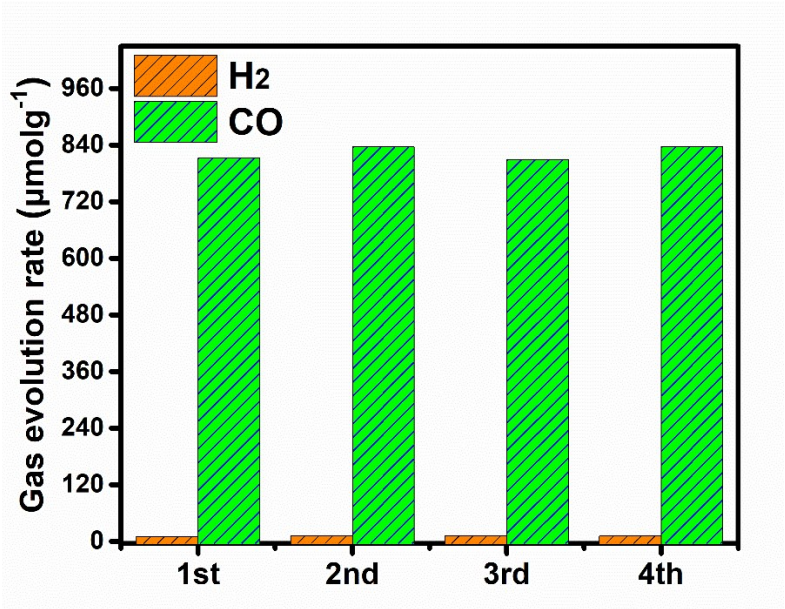

Fig. S24. Four cycle experiments for photocatalytic CO_2 reduction by using HCNT-NA for every 4h.

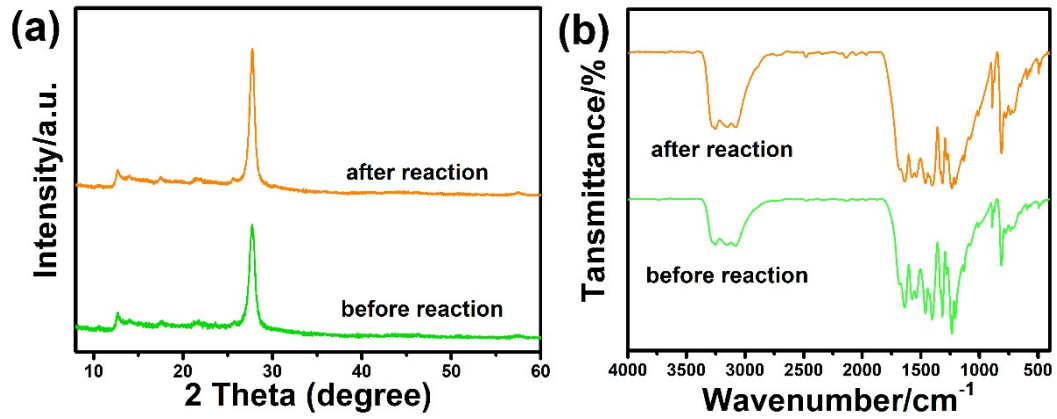

Fig. S25. (a) XRD and (b) FTIR spectra of HCNT-NA before and after the photocatalytic CO_2 reduction reaction.

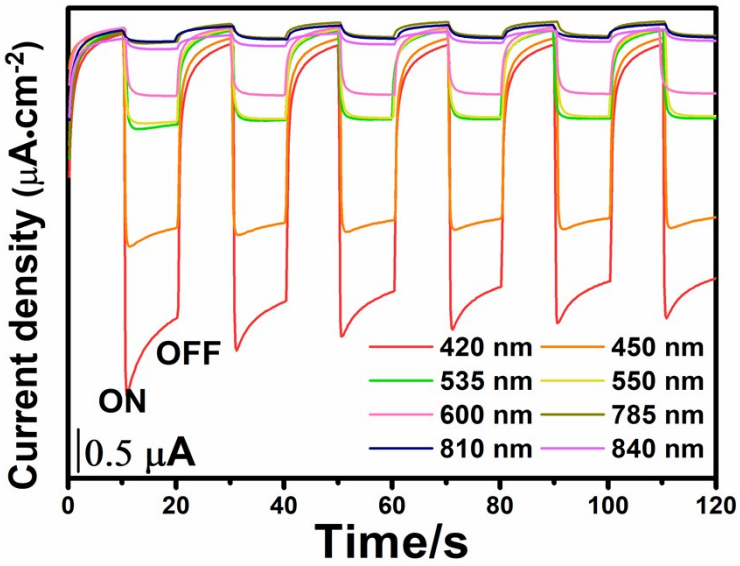

Fig. S26. Photocurrent response (bias voltage: -0.2V vs. Ag/AgCl), irradiated by different monochromatic wavelengths of 420 nm, 450 nm, 535 nm, 550 nm, 600 nm, 730 nm, 765 nm and 810 nm over HCNT-NA.

Table S2. Comparison of photocatalytic CO_2 conversion performance of previously reported typical materials and our catalyst in this work.

Catalyst	products	Normalized evolution rate ($\mu mo \cdot h^{-1} \cdot g^{-1}$)	Enhanced rates[a]	AQE (%) (λ= 420 nm)	Ref.
HCNT-NA	CO	209.24	39.5-folds	5.26	This work
MP-TAP-CVs	CO	54.6	45-folds	4.8	5
CCN	$C_nH_{2n+2}O_x$	12.07	-	-	6
mpgCN-CoPPc	CO	13.54	-	-	7
Pt/o-PCN	CO	286	34-folds	3.34	8
Fe(qpy)/C_3N_4	CO	91.2	-	4.2	9
RuRu'/Ag/NS-C_3N_4	HCOOH	83.3	-	-	10
NUZ/HGN-35%	CO	31.6	3-folds	-	11
α-Fe_2O_3/g-C_3N_4	CO	27.2	2.2-folds	0.96	12
g-C_3N_4@hm-$C(CN)_3$	CO	16.5	7.8-folds	-	13
4S-SSHoMSs-12 h)	CO/O_2	48.01	3.37-folds	-	14
V_S-$CuIn_5S_8$	CH_4	8.7	5.4-folds	0.786	15
Co–Bi_3O_4Br	CO	107.1	32-folds	-	16
3D-ZIS	CO	276.7	19-folds	-	17
Cs_2SnI_6/SnS_2	CH4	6.09	10.6-folds	-	18
MIL-101(Cr)−Ag	CO	808.2	27.3-folds	-	19

a: compared to the pristine CN matrix

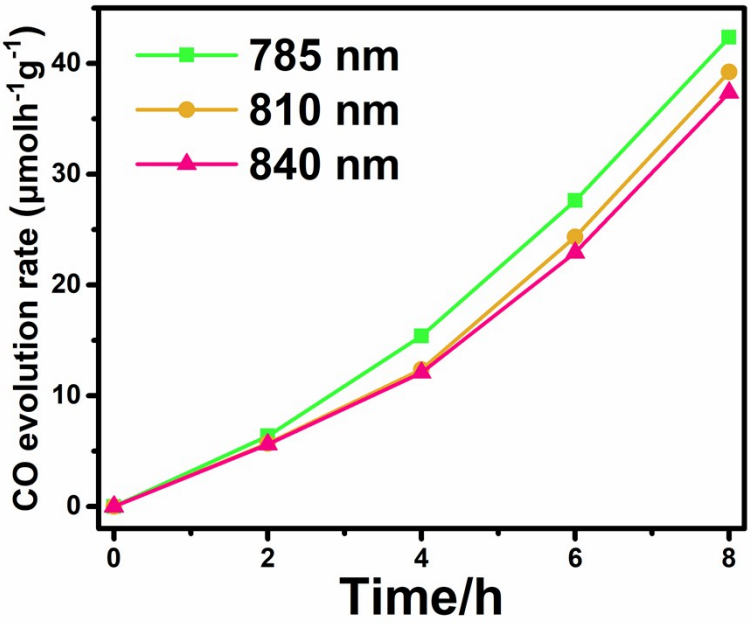

Fig. S27. Time-dependent of CO evolution at the near-infrared region such as λ=785 nm, 810 nm and 840 nm over HCNT-NA. By using BCN as a catalyst, we can't detect any products at λ=765 nm and 810 nm.

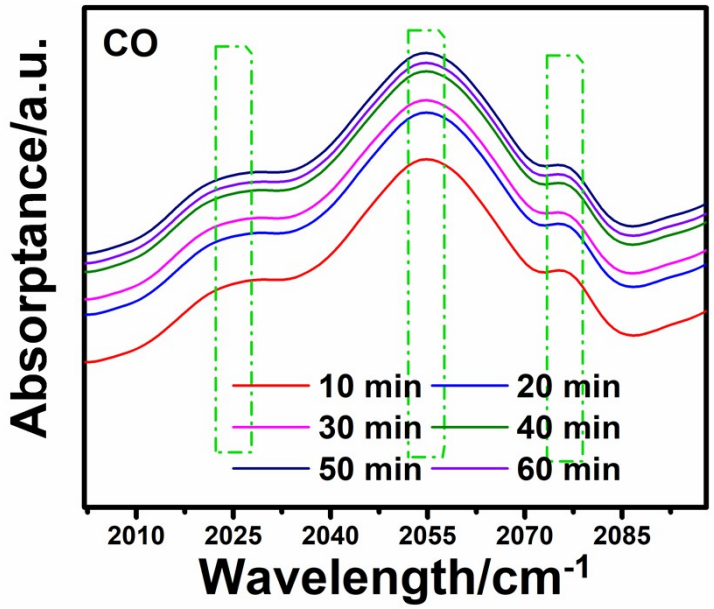

Fig. S28. In situ IR spectra of characteristic adsorption peak of CO at 2054 cm^{-1} on HCNT-NA.

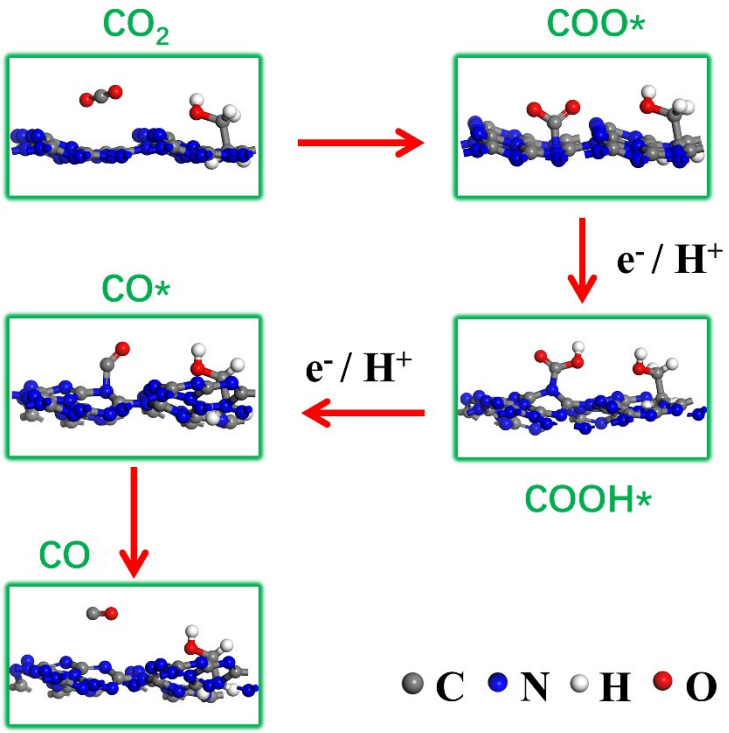

Fig. S29. Side view of each CO_2 reduction intermediate on HCNT-NA

Table S3. The free energy (eV) of each CO_2 reduction intermediate path in the pristine BCN and HCNT-NA.

	CO2	COO*	COOH*	CO*	CO
BCN	0	-0.1866	0.6821	0.4365	0.2507
HCNT-NA	0	-0.2915	0.5618	0.3673	0.2507

5. References

1. Lotsch, B. V.; Schnick, W., New Light on an Old Story: Formation of Melam during Thermal Condensation of Melamine. *Chem. Eur. J.* **2007,** *13* (17), 4956-4968.
2. Gelderman, K.; Lee, L.; Donne, S. W., Flat-Band Potential of a Semiconductor: Using the Mott–Schottky Equation. *J. Chem. Educ.* **2007,** *84* (4), 685.
3. Yu, H.; Shi, R.; Zhao, Y.; Bian, T.; Zhao, Y.; Zhou, C.; Waterhouse, G. I. N.; Wu, L.-Z.; Tung, C.-H.; Zhang, T., Alkali-Assisted Synthesis of Nitrogen Deficient

Graphitic Carbon Nitride with Tunable Band Structures for Efficient Visible-Light-Driven Hydrogen Evolution. *Adv. Mater.* **2017,** *29* (16), 1605148.
4. Zhang, J.; Zhang, M.; Yang, C.; Wang, X., Nanospherical Carbon Nitride Frameworks with Sharp Edges Accelerating Charge Collection and Separation at a Soft Photocatalytic Interface. *Adv. Mater.* **2014,** *26* (24), 4121-4126.
5. Yang, P.; Zhuzhang, H.; Wang, R.; Lin, W.; Wang, X., Carbon Vacancies in a Melon Polymeric Matrix Promote Photocatalytic Carbon Dioxide Conversion. *Angew. Chem. Int. Ed.* **2019,** *131*, 1146.
6. Xia, P.; Antonietti, M.; Zhu, B.; Heil, T.; Yu, J.; Cao, S., Designing Defective Crystalline Carbon Nitride to Enable Selective CO_2 Photoreduction in the Gas Phase. *Adv. Func. Mater.* **2019,** *29* (15), 1900093.
7. Roy, S.; Reisner, E., Visible-Light-Driven CO_2 Reduction by Mesoporous Carbon Nitride Modified with Polymeric Cobalt Phthalocyanine. *Angew. Chem. Int. Ed.* **2019,** *131* (35), 12308-12312.
8. Li, A.; Cao, Q.; Zhou, G.; Schmidt, B. V. K. J.; Zhu, W.; Yuan, X.; Huo, H.; Gong, J.; Antonietti, M., Three-Phase Photocatalysis for the Enhanced Selectivity and Activity of CO_2 Reduction on a Hydrophobic Surface. *Angew. Chem. Int. Ed.* **2019,** *58* (41), 14549-14555.
9. Cometto, C.; Kuriki, R.; Chen, L.; Maeda, K.; Lau, T.-C.; Ishitani, O.; Robert, M., A Carbon Nitride/Fe Quaterpyridine Catalytic System for Photostimulated CO_2-to-CO Conversion with Visible Light. *J. Am. Chem. Soc.* **2018,** *140* (24), 7437-7440.
10. Kuriki, R.; Yamamoto, M.; Higuchi, K.; Yamamoto, Y.; Akatsuka, M.; Lu, D.; Yagi, S.; Yoshida, T.; Ishitani, O.; Maeda, K., Robust binding between carbon nitride nanosheets and a binuclear ruthenium (II) complex enabling durable, selective CO_2 reduction under visible light in aqueous solution. *Angew. Chem. Int. Ed.* **2017,** *56* (17), 4867-4871.
11. Wang, Y.; Guo, L.; Zeng, Y.; Guo, H.; Wan, S.; Ou, M.; Zhang, S.; Zhong, Q., Amino-Assisted NH2-UiO-66 Anchored on Porous g-C_3N_4 for Enhanced Visible-Light-Driven CO2 Reduction. *ACS Appl. Mater. Interfaces.* **2019,** *11* (34), 30673-30681.
12. Jiang, Z.; Wan, W.; Li, H.; Yuan, S.; Zhao, H.; Wong, P. K., A Hierarchical Z-Scheme α-Fe2O3/g-C3N4 Hybrid for Enhanced Photocatalytic CO_2 Reduction. *Adv. Mater.* **2018,** *30* (10), 1706108.
13. Yang, Y.; Tang, Z.; Zhou, B.; Shen, J.; He, H.; Ali, A.; Zhong, Q.; Xiong, Y.; Gao, C.; Alsaedi, A.; Hayat, T.; Wang, X.; Zhou, Y.; Zou, Z., In Situ No-slot Joint Integration of Half-Metallic $C(CN)_3$ Cocatalyst into g-C_3N_4 Scaffold: an Absolute Metal-Free In-Plane Heterosystem for Efficient and Selective Photoconversion of CO_2 into CO. *Appl. Catal., B.* **2019**, 118470.
14. You, F.; Wan, J.; Qi, J.; Mao, D.; Yang, N.; Zhang, Q.; Gu, L.; Wang, D., Lattice Distortion in Hollow Multi-Shelled Structures for Efficient Visible Light CO_2 Reduction with a SnS_2/SnO_2 Junction. *Angew. Chem. Int. Ed.* **2019,** 13,1-5.

15. Li, X.; Sun, Y.; Xu, J.; Shao, Y.; Wu, J.; Xu, X.; Pan, Y.; Ju, H.; Zhu, J.; Xie, Y., Selective visible-light-driven photocatalytic CO_2 reduction to CH_4 mediated by atomically thin CuIn5S8 layers. *Nat. Energy.* **2019,** *4* (8), 690-699.
16. Di, J.; Chen, C.; Yang, S.-Z.; Chen, S.; Duan, M.; Xiong, J.; Zhu, C.; Long, R.; Hao, W.; Chi, Z., Isolated single atom cobalt in Bi_3O_4Br atomic layers to trigger efficient CO_2 photoreduction. *Nat. Commun.* **2019,** *10* (1), 1-7.
17. He, Y.; Rao, H.; Song, K.; Li, J.; Yu, Y.; Lou, Y.; Li, C.; Han, Y.; Shi, Z.; Feng, S., 3D Hierarchical $ZnIn_2S_4$ Nanosheets with Rich Zn Vacancies Boosting Photocatalytic CO_2 Reduction. *Adv. Funct. Mater.* **2019,** *29* (45), 1905153.
18. Wang, X.-D.; Huang, Y.-H.; Liao, J.-F.; Jiang, Y.; Zhou, L.; Zhang, X.-Y.; Chen, H.-Y.; Kuang, D.-B., In Situ Construction of a Cs_2SnI_6 Perovskite Nanocrystal/SnS_2 Nanosheet Heterojunction with Boosted Interfacial Charge Transfer. *J. Am. Chem. Soc.* **2019,** *141* (34), 13434-13441.
19. Guo, F.; Yang, S.; Liu, Y.; Wang, P.; Huang, J.; Sun, W.-Y., Size Engineering of Metal–Organic Framework MIL-101(Cr)–Ag Hybrids for Photocatalytic CO_2 Reduction. *ACS Catal.* **2019,** *9* (9), 8464-8470.